

The study of flux redistribution during molecular photodissociation: Adiabatic and diabatic analyses and application to the dissociation of CH₃I

Millard H. Alexander, Claire Rist, and David E. Manolopoulos

Citation: *The Journal of Chemical Physics* **97**, 4836 (1992); doi: 10.1063/1.463838

View online: <http://dx.doi.org/10.1063/1.463838>

View Table of Contents: <http://scitation.aip.org/content/aip/journal/jcp/97/7?ver=pdfcov>

Published by the **AIP Publishing**

Articles you may be interested in

[Flux redistribution during the photodissociation of CINO in the T 1 state](#)

J. Chem. Phys. **101**, 4722 (1994); 10.1063/1.467395

[Adiabatic representations for the study of flux redistribution during photodissociation involving coupled electronic states: The effect of vibrational excitation on the photofragmentation of CH₃I](#)

J. Chem. Phys. **98**, 6196 (1993); 10.1063/1.464813

[Quantum flux redistribution during molecular photodissociation](#)

J. Chem. Phys. **97**, 2527 (1992); 10.1063/1.463091

[Molecular coherences in collisional redistribution and photodissociation](#)

AIP Conf. Proc. **216**, 255 (1990); 10.1063/1.39967

[The eikonal approximation to molecular photodissociation: Application to CH₃I](#)

J. Chem. Phys. **90**, 5501 (1989); 10.1063/1.456455



The study of flux redistribution during molecular photodissociation: Adiabatic and diabatic analyses and application to the dissociation of CH₃I

Millard H. Alexander and Claire Rist

Department of Chemistry and Biochemistry, University of Maryland, College Park, Maryland 20742

David E. Manolopoulos

Department of Chemistry, University of Nottingham, University Park, Nottingham NG7 2RD, United Kingdom

(Received 17 March 1992; accepted 18 June 1992)

This paper extends our new method for the study of the mechanism of molecular photodissociation. This method involves the time-independent study of the growth of photofragment flux, governed by photon absorption, and the subsequent redistribution of the flux, governed by the Hamiltonian in the excited, unbound state. The flux analysis can be carried out easily in either a diabatic (asymptotic), locally adiabatic, or fully adiabatic basis. The redistribution of the photofragment flux can be investigated in either internal state space or coordinate space at each excitation energy. Application is made to one- and two-dimensional models for the photodissociation of CH₃I.

I. INTRODUCTION

There has been extensive theoretical interest in the mechanism of molecular photodissociation. In the time-independent approach,¹⁻⁸ determination of the transition probabilities for photoexcitation from an initial bound state to any particular unbound state involves solution of the same close-coupled equations which arise in the description of inelastic molecular scattering.^{9,10} Recently,¹¹ we have reinvestigated a particular formulation, due originally to Band, Freed, and Kouri,¹² in which the transition probabilities can be obtained from the asymptotic expansion of the solution to certain inhomogeneous first-order perturbation equations. Our interest in this approach stems from the physical interpretation which can be associated with this wave function, which rises from zero at small interparticle distance and becomes a linear combination of purely outgoing waves asymptotically. The current density associated with this wave function can provide a direct probe of the mechanism of the photodissociation. Flux rises in the various channels of the unbound excited state as the initially bound fragments move through the region where the photon is absorbed, and then is redistributed because of interactions in the excited state. The study of the redistribution of flux accompanying molecular photodissociation is a logical complement to the recent study of the redistribution of flux accompanying inelastic molecular collisions.^{13,14}

The time-independent flux method provides a wealth of mechanistic information on the dependence of the photodissociation process on the interfragment separation. This mechanistic information yields an altogether different, but complementary, point of view to that given by the well-established time-dependent wave packet approach to photodissociation,¹⁵⁻²⁷ due originally to Heller and co-workers.^{15-17,28} In most applications of the time-dependent approach, mechanistic information, albeit without energy resolution, is afforded by the study of the motion of a prepared wave packet on the excited, dissociative potential

surface. An alternative approach, in which dynamical information at a particular energy of interest can be obtained from a time-dependent method, has been proposed by Frederick *et al.*,²⁹ but has not yet (to the best of our knowledge) been applied to a bound \rightarrow continuum process.

In our application of the flux method to the study of molecular photodissociation, we use a log-derivative algorithm³⁰⁻³⁶ for determination of both the homogeneous³¹⁻³⁴ and inhomogeneous^{34,37,38} propagators necessary in the solution of the inhomogeneous equations which arise in the driven equation approach of Band, Freed, and Kouri.¹² The flux analysis in our original paper was carried out in the asymptotic (diabatic) basis used to expand the photofragmentation wave function. In the present paper, we show how a similar analysis can be carried out in either a locally adiabatic or fully adiabatic basis and explore the relationship between these. Flux analysis in a locally adiabatic basis would be a natural byproduct of the use of an "approximate potential" propagation method,¹⁰ in which one determines the *exact* scattering wave function for an *approximate* potential. Such a method is particularly advantageous for photodissociation problems where a substantial fraction of the photon energy is released into kinetic energy of the fragments. In this case, the local deBroglie wavelength of the dissociating fragments is small, so that the number of steps which must be taken in an "approximate solution" method becomes large.

The organization of the present paper is as follows: in the next section, we review briefly the driven equation approach to molecular photodissociation¹² and the log-derivative propagation method for solution.^{11,34,37,38} Sections III and IV outline the determination of the photofragment flux, within either an asymptotic, locally adiabatic, or fully adiabatic basis. Section V presents the application of the flux method to the photodissociation of CH₃I based on one- and two-dimensional models for this process that have been used in several prior studies.^{4,26,27} A brief conclusion follows.

II. CLOSE-COUPLED EQUATIONS

In the present paper, we shall limit ourselves to those general equations which are specifically necessary in the subsequent discussion of the flux analysis in the diabatic, locally adiabatic, and fully adiabatic bases. More detail on the application of log-derivative propagation schemes in the driven equation approach to molecular photodissociation¹² can be found in our previous article,¹¹ as well as in earlier papers of Mrugala^{37,38} and Manolopoulos.³⁴

The photodissociation amplitude can be obtained from the solution $\psi(R)$ to a set of inhomogeneous equations. These are, in matrix notation,

$$\left[\frac{d^2}{dR^2} + W(R) \right] \psi(R) = \chi(R), \quad (1)$$

where $W(R) = k^2 - l(l+1) - V(R)$ is the wave vector matrix of the excited (unbound) electronic potential. The solution vector $\psi(R)$ in Eq. (1) contains the coefficients in the expansion of the wave function for the dissociating molecule in terms of a complete set of internal states of the isolated fragments, namely,

$$\Psi(R, r) = \frac{1}{R} \sum_n \psi_n(R) \phi_n(r), \quad (2)$$

where r designates the collective internal coordinates and $\phi_n(r)$ designates an eigenvector of the Hamiltonian of the isolated fragments. Finally, in Eq. (1) $\chi(R)$ is a column vector with elements proportional to the vibrational wave function of the electronic ground state multiplied by the bound-free transition dipole moment

$$\chi_n(R) = \frac{2\mu}{\hbar^2} \int \phi_n(r) \bar{\epsilon} \cdot \bar{D}(r, R) R \phi_g(r, R) dr, \quad (3)$$

where $\bar{\epsilon}$ is the electric field vector of the excitation laser and $\bar{D}(r, R)$ is the transition dipole moment.

Equation (1) is solved subject to the following boundary conditions on the column vector solution $\psi(R)$:

$$\lim_{R \rightarrow 0} \psi(R) = 0 \quad (4)$$

and

$$\lim_{R \rightarrow \infty} \psi(R) = O(R) \tau. \quad (5)$$

Here $O(R)$ is a diagonal matrix of flux normalized outgoing wave components in each fragment channel, the elements of which are proportional to Riccati-Hankel functions.³⁹ The n th row of the column vector τ gives the amplitude for dissociative excitation into internal state n of the fragments.

The values of the vector $\psi(R)$ at any two values of the interparticle distance (a and b , say) are related by the fundamental log-derivative propagation relation [Eq. (A5) of Ref. 11]. This propagation relation involves the same real log-derivative propagators which appear in the standard close-coupled equations for inelastic molecular scattering,^{10,30-34,37} in addition to two inhomogeneous propagators which are defined by^{34,37}

$$\lambda_1(a, b) = - \int_a^b \psi_+(R)^T \chi(R) dR \quad (6a)$$

and

$$\lambda_2(a, b) = + \int_a^b \psi_-(R)^T \chi(R) dR. \quad (6b)$$

Here $\psi_+(R)$ and $\psi_-(R)$ are matrices representing real solutions to the homogeneous (scattering) equations

$$\left[\frac{d^2}{dR^2} + W(R) \right] \psi_{\pm}(R) = 0 \quad (7)$$

with boundary conditions

$$\begin{bmatrix} \psi_+(a) & \psi_-(a) \\ \psi_+(b) & \psi_-(b) \end{bmatrix} = \begin{pmatrix} -1 & 0 \\ 0 & +1 \end{pmatrix}. \quad (8)$$

In practice, Eq. (1) is solved numerically by breaking up the range of integration into a number of sectors. Determination of the photodissociation amplitude τ [Eq. (5)] requires knowledge of the behavior of the homogeneous and inhomogeneous log-derivative propagators over the full range of R .^{11,34} These propagators can be accumulated in a straightforward manner as one moves outward from sector to sector using the relationships given in Eqs. (A13)–(A16) of Ref. 11.

In an “approximate potential algorithm,”^{10,40-42} in each sector the photodissociation wave function is expanded not in the asymptotic states $\phi(r)$, but rather in a set of *locally adiabatic* states $\tilde{\phi}(r)$, which we designate by a tilde superscript. The relationship between the two bases is given by an orthogonal transformation

$$\tilde{\phi}(r) = T \phi(r), \quad (9)$$

where the transformation matrix T is chosen to diagonalize the wave vector matrix $[W(R)$ in Eq. (1)] at the midpoint of each sector ($R=c$). That is,

$$T W(c) T^T = \tilde{k}^2 \quad (10)$$

with \tilde{k} designating the diagonal matrix of local wave vectors for the particular sector.

In the locally adiabatic basis, the expansion of the wave function can be written, analogously to Eq. (2), as

$$\Psi(R, r) = \frac{1}{R} \sum_n \tilde{\psi}_n(R) \tilde{\phi}_n(r), \quad (11)$$

where the two column vectors of expansion coefficients satisfy the relation

$$\tilde{\psi}(R) = T \psi(R). \quad (12)$$

Within the sector, the locally adiabatic solutions to the homogeneous equation satisfy the equation

$$\left[\frac{d^2}{dR^2} + \tilde{k}^2 + (R-c) \tilde{W}' + \cdots \right] \tilde{\psi}_{\pm}(R) = 0, \quad (13)$$

where

$$\tilde{W}' = T W'(R) \Big|_{R=c} T^T \quad (14)$$

and we have retained terms only up through linear in $W(R)$.

In the locally adiabatic basis, we designate the inhomogeneous propagators as $\tilde{\lambda}_m$. These are defined identically to Eq. (6), except that the column vector $\chi(R)$ which appears in the integration is expressed in the locally adiabatic basis. In other words,

$$\tilde{\lambda}_m(a,b) = \mp \int_a^b \tilde{\psi}_{\pm}(R)^T \tilde{\chi}(R) dR. \quad (15)$$

Here $\tilde{\psi}_{\pm}(R)$ are the solutions to Eq. (13) which obey the boundary conditions of Eq. (8).

In the particular implementation of the “approximate potential” algorithm used in the calculations to be presented below, we retained only the *diagonal* terms in the \tilde{W} matrix. This defines a set of *uncoupled* “linear reference” equations,¹⁰ first introduced by Gordon.^{40,41,43} The use of a linear reference potential in the solution of Eq. (1) can be seen as an extension of earlier work of Gordon⁴³ on the solution of inhomogeneous equations. Our approach differs by making use of log-derivative, rather than Cauchy, propagators.^{31,34} In prior work we have discussed the calculation of the requisite homogeneous propagators.⁴² The technical details of the determination of the required inhomogeneous propagators will be deferred until a subsequent publication.⁴⁴

III. FLUX REDISTRIBUTION

From a knowledge of the solution $\psi(R)$ to Eq. (1), it is possible to follow directly the growth of flux in the unbound, excited state as the photon is absorbed and the subsequent redistribution of this flux among the internal states of the system as the fragments separate.¹¹ The formal development starts by expressing the current density through the surface R_0 as the expectation value of the flux operator

$$J(R_0) = \langle \Psi(r; R) | F(R_0) | \Psi(r; R) \rangle, \quad (16)$$

where the operator $F(R_0)$ is given by Miller, Tromp, and Schwarz^{45,46}

$$F(R_0) = \frac{-i\hbar}{2\mu R} \left[\frac{d}{dR} \delta(R - R_0) + \delta(R - R_0) \frac{d}{dR} \right] R. \quad (17)$$

Explicitly introducing Eq. (2), and integrating over R , we find

$$J(r; R_0) dr = \frac{\hbar}{\mu} \text{Im} \sum_{n,m} \psi_m(R_0) * \phi_m(r) * \psi'_n(R_0) \phi_n(r) dr, \quad (18)$$

which represents the outgoing flux at point R_0 associated with internal coordinate r . Here we have introduced the notation

$$\left. \frac{d}{dR} f(R) \right|_{R=R_0} \equiv f'(R_0) \quad (19)$$

for simplicity in what follows.

Integration of Eq. (18) over r gives the total flux $J(R_0)$ as a sum over the components of a column vector

whose n th element is the photofragment flux associated with internal state n at internuclear separation R , namely

$$J(R_0) = \sum_n J_n(R_0), \quad (20)$$

where

$$J_n(R_0) = \frac{\hbar}{\mu} \text{Im} [\psi_n(R_0) * \psi'_n(R_0)]. \quad (21)$$

Our definition of the flux here is consistent with the convention that a *positive* sign corresponds to flux directed outward (toward increasing R). From Eqs. (5) and (21), and the fact that $O(R_0) * O'(R_0) = \mu/\hbar$,¹¹ we conclude that

$$\lim_{R_0 \rightarrow \infty} J_n(R_0) = |\tau_n|^2. \quad (22)$$

Thus the components of the column vector τ which appears in Eq. (5) can be designated *flux amplitudes*.

Equation (20) expresses the total flux in terms of the asymptotic (diabatic) basis. Similarly, we can expand the total flux in the locally adiabatic basis, namely

$$J(R_0) = \sum_n \tilde{J}_n(R_0), \quad (23)$$

where

$$\tilde{J}_n(R_0) = \frac{\hbar}{\mu} \text{Im} [\tilde{\psi}_n(R_0) * \tilde{\psi}'_n(R_0)]. \quad (24)$$

Because the transformation between the locally adiabatic and diabatic basis is orthogonal, the total flux is conserved by this diabatic \rightarrow adiabatic transformation,¹³ as would be expected on physical grounds.

After determination of the vector τ , and hence the asymptotic flux, the previously calculated propagators can be used to determine the flux at the inward boundary of each sector. Within the “approximate potential” method advocated here, this involves (1) transforming the wave function at the outer boundary of the sector into the locally adiabatic basis using the sector transformation matrix T ; (2) using the back substitution algorithm defined in the Appendix to Ref. 11 to determine the wave function and its derivative at the inner boundary of the sector (still in the locally adiabatic basis); (3) determining the flux in the locally adiabatic basis at the inner boundary from Eq. (24); and then (4) transforming the wave function at the inner boundary into the asymptotic basis using the transpose of the sector transformation matrix. Determination of the flux in the asymptotic, rather than the locally adiabatic, basis can be achieved by inverting steps (3) and (4).

We shall assume that the outgoing waves in Eq. (5) are normalized by the square root of the channel velocities,¹¹ rather than the square root of the asymptotic channel wave vectors, as is usual in the theory of inelastic molecular collisions.¹⁰ If so, and since the ground state wave function $\phi_g(R)$ has dimensions $\text{length}^{-1/2}$, one can show easily that the dimensions of τ will be $\text{time}^{-1/2}$.⁴⁷ If atomic units are used throughout, the calculated value of J will be equal to the number of dissociating molecules per atomic unit of time (2.419×10^{-17} s) for an excitation laser of

electric field strength of one atomic unit (5.142×10^9 V/cm). From Eq. (22), we conclude that the calculated channel fluxes represent the number of dissociating fragments in internal state n which would be detected in 1 a.u. of time by a hypothetical state detector placed at interfragment separation R (for an excitation laser of unit electric field strength).

IV. FLUXES IN FULLY AND LOCALLY ADIABATIC BASES

Analogously to Eq. (9), it is possible to define a *fully adiabatic* basis

$$\phi^a(r; R) = T(R)\phi(r), \quad (25)$$

where $T(R)$ is the matrix which continuously diagonalizes the $W(R)$ matrix at each value of R . In the fully adiabatic basis, the expansion coefficients of the dissociative wave function are given by, similarly to Eq. (12),

$$\psi^a(R) = T(R)\psi(R). \quad (26)$$

Equation (25) can be inverted to yield

$$\phi(r) = T(R)^T \phi^a(r; R). \quad (27)$$

Substitution of this expression into Eq. (18) and integration over r gives, where the matrix and column vector indices have been introduced explicitly,

$$J(R_0) = \frac{\hbar}{\mu} \text{Im} \sum_{m,n} \int_{r,s} \left\{ \psi_s(R_0)^* T_{rs}(R_0) \phi_r^a(r; R)^* \right. \\ \left. \times \frac{d}{dR} [\psi_n(R) T_{mn}(R) \phi_m^a(r; R)]_{R=R_0} \right\} dr. \quad (28)$$

We have assumed here that the $W(R)$ matrix is real symmetric, as is usually the case, so that the transformation matrices $T(R)$ are real orthogonal.

Of the three terms in the derivative inside the integral sign in Eq. (28), two cancel, because from Eq. (27)

$$\frac{d}{dR} \phi(r) = 0 = \frac{d}{dR} T(R)^T \phi^a(r; R). \quad (29)$$

Taking this into account, and using the orthogonality of the adiabatic states, we can reduce Eq. (28) to

$$J(R_0) = \frac{\hbar}{\mu} \text{Im} \sum_{m,n} \psi_n(R_0)^* T_{mn}(R_0) \psi'_n(R_0) T_{mn}(R_0). \quad (30)$$

Thus the orthogonality of the transformation matrix $T(R)$ implies

$$J(R_0) = \sum_m J_m^a(R_0), \quad (31)$$

where

$$J_m^a(R_0) = \frac{\hbar}{\mu} \text{Im} [\psi_m^a(R_0)^* \psi'_m(R_0)] \quad (32)$$

with

$$\psi^a(R_0) = T(R_0)\psi(R_0) \quad (33)$$

and similarly for $\psi'^a(R_0)$.

In the locally adiabatic basis, the channel fluxes are given by Eq. (32), except that the expansion coefficients of the wave function are defined by

$$\tilde{\psi}(R_0) = T(R_c)\psi(R_0) \quad (34)$$

and similarly for $\tilde{\psi}'(R_0)$. Here c is the midpoint of the sector in which the point R_0 falls. As the sector width h decreases, we have

$$\lim_{h \rightarrow 0} T(c) = T(R_0). \quad (35)$$

Thus by comparison of Eqs. (34) and (35), as well as Eqs. (24) and (32), we come to the important conclusion that the locally adiabatic channel components of the flux will approach the fully adiabatic channel components as the sector width decreases to zero.

Finally, it should be noted that this analysis of the outgoing photofragment flux in an adiabatic basis may well be more meaningful for problems which are strongly coupled in the final state than the diabatic basis flux analysis used in Ref. 11. The individual diabatic channel fluxes give a direct measure of the probabilities associated with each diabatic channel as a function of R_0 , as indicated by their asymptotic forms in Eq. (22). Since the wave vector matrix $W(R)$ eventually becomes diagonal at large R , the diabatic and adiabatic bases eventually become the same, and a similar interpretation obtains for the adiabatic channel flux components. Extending this interpretation inwards to smaller R_0 , we obtain a picture which quantifies the extent to which a given photodissociation event can be regarded as electronically and/or rovibrationally adiabatic in any final state. In particular, the idealized situation in which there is absolutely no flux redistribution between the adiabatic channels outside the Franck-Condon region corresponds to a perfectly adiabatic final state fragmentation, or, in the terminology introduced by Schinke,⁴⁸ dissociation with no final state interactions.

V. DEMONSTRATION CALCULATIONS

As a first test of the method presented here, we chose the same two-state model for the photodissociation of CH_3I presented by Guo and Schatz²⁷ which was studied in our previous article¹¹ on the study of flux redistribution using an approximate solution algorithm to solve the driven equations. In this model, the $^3Q_{0+}$ and 1Q_1 states of CH_3I are approximated by two one-dimensional curves, which correlate at large R with, respectively, the upper ($\text{CH}_3 + \text{I}^*$) and lower energy ($\text{CH}_3 + \text{I}$) dissociation channels. These curves are shown in Fig. 1 of Ref. 11 and the relevant parameters are given in Refs. 11 and 27. Following these prior papers, we allow simultaneous excitation to both the $^3Q_{0+}$ and 1Q_1 states.

The upper panel of Fig. 1 displays the outgoing flux in the *adiabatic* states which correlate at long range with, respectively, the I^* and I channels, for a total collision energy of 0.1 hartree. The solid curves were determined

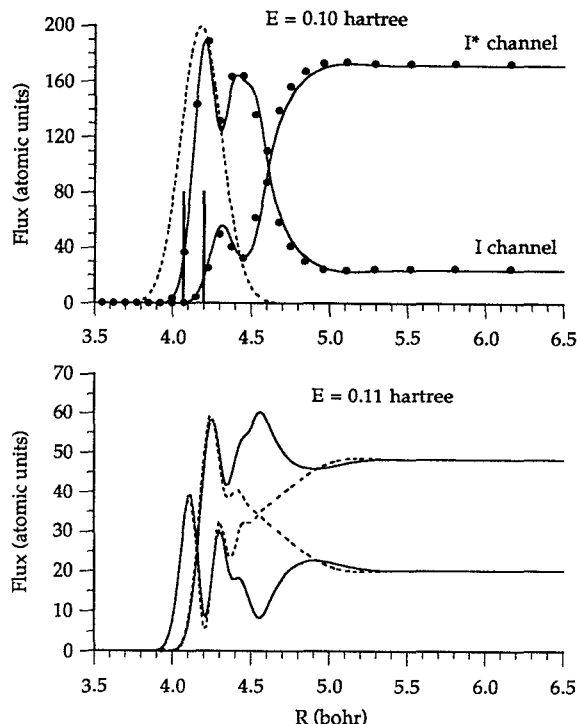


FIG. 1. (Upper panel) The one-dimensional model of CH_3I photodissociation (Ref. 27). The predicted outgoing flux in the *adiabatic* states which correlate at long range with, respectively, the I^* and I channels, for an energy of 0.1 hartree (with respect to the $\text{CH}_3 + \text{I}$ channel). Excitation to both the $^3Q_{0+}$ and 1Q_1 states was assumed with the dipole moment functions of Ref. 27. The solid curves represent a calculation using 384 sectors of width 0.012 bohr ranging from 3.4 to 8 bohr. The filled circles represent the results of a calculation using 28 sectors of variable width ranging from 0.075 bohr at short range and increasing geometrically after $R=4.5$ bohr by a constant factor of 1.25. The dashed curve is a scaled representation of the component of the source function $\chi(R)$ associated with the $^3Q_{0+}$ channel. The classical turning points of the lower and upper adiabatic states are indicated by the heavy vertical lines. (Lower panel) Outgoing fluxes in both the *adiabatic* (solid curves) and *diabatic* (dashed curves) bases at an energy of 0.11 hartree. All other parameters were identical to those used in the calculation for the upper panel.

using 384 sectors between 3.4 and 8 bohr, with a constant sector width of 0.012 bohr (the asymptotic value of the deBroglie wavelength in the channel with greater kinetic energy is 0.090 bohr). The power of the linear reference potential method is illustrated by the filled circles, which represent the results of a calculation, again ranging from 3.4 to 8 bohr, with an initial step size of 0.075 bohr, which was allowed to increase by a constant geometric factor of 1.25 once R became greater than 4.75 bohr. The number of sectors used was only 28. Despite the drastic reduction in the number of sectors, the predicted flux still mirrors the more accurate value, with virtually quantitative accuracy. This drastic economy in the number of required sectors illustrates the power of the linear reference potential propagation, particularly for systems in which the coupling potentials are longer ranged than the Gaussian coupling in the Guo-Schatz model.

Also displayed in the upper panel to Fig. 1 is the component of the source function $\chi(R)$ in the $^3Q_{0+}$ state scaled to size. One can see clearly the rise in flux associated

with absorption of the photon, followed, at larger values of R , by the redistribution of the flux accompanying the non-adiabatic interactions in the dissociating molecule. As might be expected, the appearance of flux in the excited states is significant only when the states have become classically allowed. The lower panel of Fig. 1 compares the outgoing fluxes in both the adiabatic and diabatic bases, for a total collision energy of 0.11 hartree. Since the Franck-Condon zone lies inside the curve-crossing region,¹¹ the picture of flux growth due to photon absorption is independent of the representation. In the curve-crossing region, however, the two pictures are complementary: In the diabatic picture, flux is transferred smoothly from the 1Q_1 curve onto the $^3Q_{0+}(\text{I}^*)$ curve as the system recedes through the crossing region. In the adiabatic picture, the flux created initially on the 1Q_1 curve (the higher energy curve in the Franck-Condon region) oscillates substantially as the system passes through the crossing, but, in overall magnitude, is transferred adiabatically onto the $^3Q_{0+}(\text{I}^*)$ curve in the asymptotic region.

A second, more complex test of the method is the two-dimensional model for the photodissociation of CH_3I , due originally to Shapiro,⁴ in which an additional internal coordinate is added, which mimics the umbrella motion of the CH_3 moiety. We use the functional forms given by Guo and Schatz²⁶ for the excited and ground CH_3I potential surfaces, $^3Q_{0+}-^1Q_1$ coupling, and dipole-moment functions, which are slight modifications of the those developed originally by Shapiro.⁴ For continuity, the potential energy surfaces for the two states, shown clearly in Fig. 1 of Ref. 26, are depicted here also in Fig. 2. Both the ground state wave function $\phi_g(r;R)$ in Eq. (5) as well as the scattering wave functions were expanded in a set of Hermite functions appropriate to the vibrational frequency of the CH_3 "mode." For the ground state function, this involved reexpansion of the function given by Guo and Schatz^{26,49} (based on earlier work of Lee and Heller⁵⁰).

Figure 3 shows the dependence on energy of the total flux into the I and I^* channels summed over fragment vibrational state. For comparison with the one-dimensional calculations presented above and in our previous paper, dipole coupling to both the $^3Q_{0+}$ and 1Q_1 electronic states was included, again using the matrix elements given by Shapiro. Figure 4 displays "flux snapshots" at three different energies encompassed in the absorption profile of Fig. 3 and corresponding to excitation at wavelengths of 276, 266, and 248 nm. These wavelengths correspond to those used in a number of recent experimental studies of the relative I^*/I yield in the CH_3I photolysis.⁵¹⁻⁵⁶ With our choice of the vibrational potential of the ground state of CH_3I ,^{26,50} these wavelengths corresponds to energies of 17 939, 19 301, and 22 029 cm^{-1} above the asymptotic energy of the $\text{CH}_3 + \text{I}$ channel.

In Fig. 4, the flux snapshots from the two-dimensional calculations are compared with those at the identical energies for the one-dimensional model of Ref. 27. Although there is some difference in the magnitude of the fluxes, particularly at longer wavelength, the one-dimensional model is seen to predict well the overall nature of the elec-

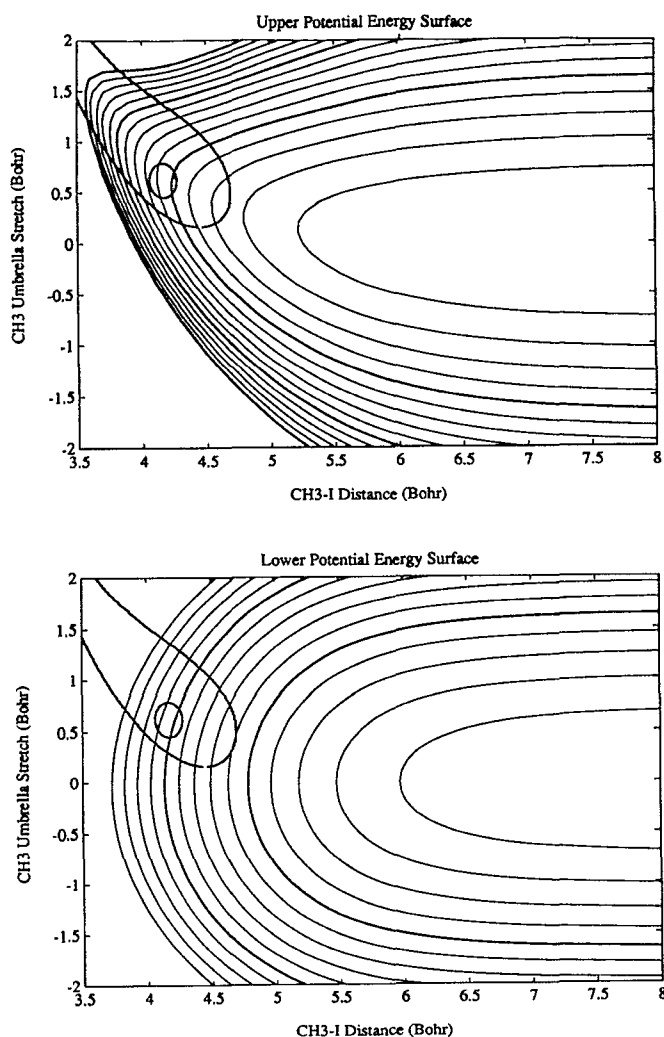


FIG. 2. Diabatic potential energy surfaces for the $^3Q_{0+}$ state (upper panel) and 1Q_1 state (lower panel) of CH_3I for the two-dimensional model of Shapiro (Ref. 4, with potentials and parameters taken from Ref. 26). The contours are spaced at 0.01 hartree intervals; for clarity, bolder contours are used at every 0.05 hartree. The minimum for the $^3Q_{0+}$ surface lies at 0.0346 hartree above the minimum for the 1Q_1 surface. The 1Q_1 surface rises above the $^3Q_{0+}$ surface within the irregular region extending downwards from the upper left corner. The half-maximum extent of the ground-state vibrational wave function is indicated by the small oval. For excitation at 266 nm, the available energy in the $^3Q_{0+}$ state is 0.0521 hartree and, in the 1Q_1 state, 0.0867 hartree.

tronic nonadiabaticity in the photolysis of CH_3I . In particular, the qualitative mechanistic conclusions of our earlier paper are seen to be still valid.¹¹ The relative population of the I and I^* channels reflects two competing effects. As the energy increases, initial population in the $^3Q_{0+}$ channel (the dominant excitation channel) is less likely to transfer to the 1Q_1 state because the curve crossing probability (in a diabatic picture) will decrease with increasing velocity.⁵⁷ On the other hand, direct excitation of the 1Q_1 state becomes increasingly probable at higher energy as the classical turning point for this state moves into and through the Franck-Condon region.

In Fig. 4, we further observe the presence of an overall undulatory flux transfer between the two states, which is

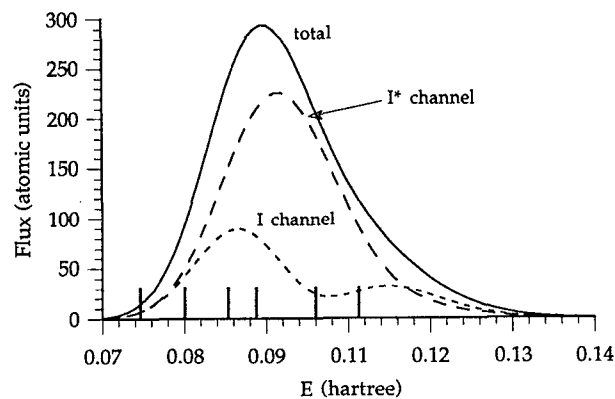


FIG. 3. Total photodissociation flux in the CH_3+I and CH_3+I^* electronic channels, summed over final-state vibrational quantum numbers, as a function of the final state energy (with the CH_3+I channel taken to define the zero of energy) for the two-dimensional model of Shapiro (Ref. 4, with potentials and parameters taken from Ref. 26). The simultaneous excitation of both the $^3Q_{0+}$ and 1Q_1 states was assumed with the dipole moment functions of Ref. 4. The vertical bars indicate the energy associated with excitation at photon wavelengths of (from lower to higher energy) 287, 276, 266, 260, 248, and 240 nm.

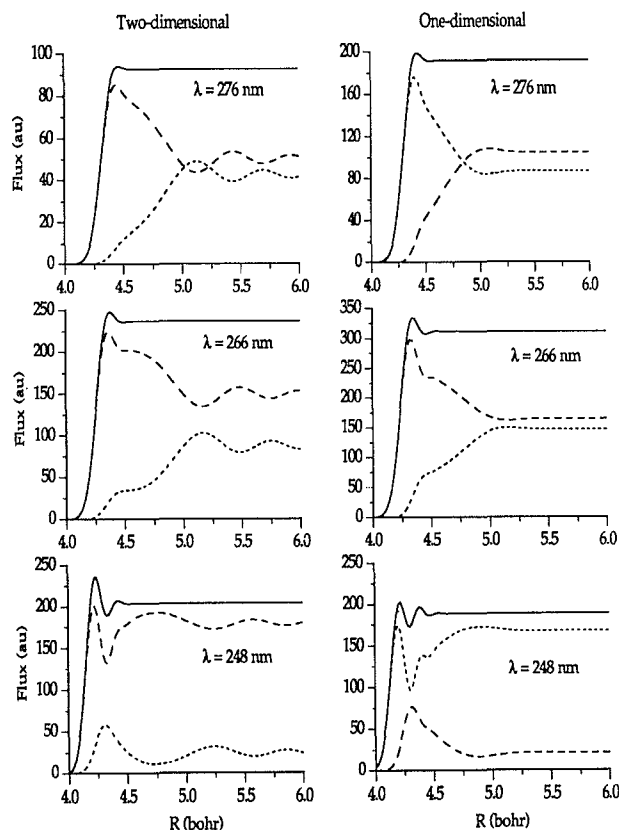


FIG. 4. "Flux snapshots"—six plots showing the dependence of the total photodissociation flux (solid curves), as well as the photodissociation flux associated with the $^3Q_{0+}(\text{I}^*)$ channel (long-dashed curves), and the $^1Q_1(\text{I})$ channel (short dashed curve), as a function of the dissociation coordinate R at three representative energies from Fig. 3. The figures on the left side are for the two-dimensional model of Shapiro (Ref. 4) as modified by Guo and Schatz (Ref. 26), while the figures on the right side are for the one-dimensional model of the latter authors. Notice that the flux scale changes from one plot to another.

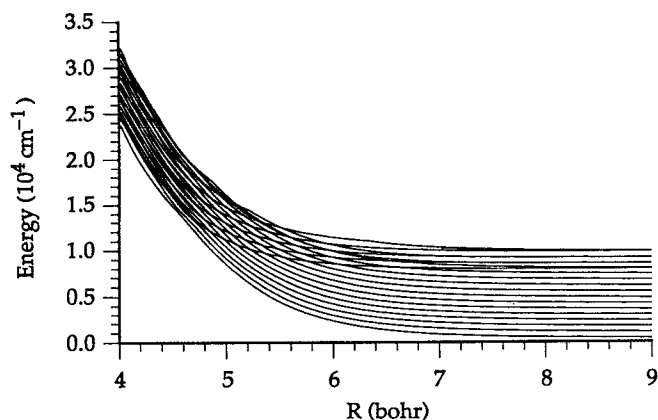


FIG. 5. A plot of the lowest 20 adiabatic energies for the two-dimensional model of CH_3I of Refs. 4 and 26. The adiabatic energies are defined in terms of the local wave vectors [Eq. (10)] as $(\hbar^2 k^2)/2\mu$.

not seen in the one-dimensional model. This arises from the presence of multiple crossings in the exit channel between various $^3Q_{0+}(v')-^1Q_1(v)$ pairs, and the persistence of the coupling between the $^3Q_{0+}$ and 1Q_1 electronic states. [In the one-dimensional model²⁷ the electronic coupling is a strongly damped gaussian, $\exp\{-5(R-4.56)^2\}$,²⁷ while in the two-dimensional model, the coupling is a more weakly damped exponential, $\exp\{-0.5(R-4.012)\}$.²⁶] In their time-dependent study of CH_3I dissociation, Guo and Schatz²⁶ observed a similarly oscillatory behavior in the $^3Q_{0+}$ component of the propagated wave packet. The mechanistic information given by a wave packet-based study is an average over myriad flux snapshots such as those in Fig. 4, weighted by the overall absorption profile (Fig. 3). However, the appearance of the oscillatory flux transfer in *all* panels of Fig. 4 suggests that this feature will indeed persist after energy averaging.

Guo and Schatz²⁶ attributed this oscillatory pattern to interference during the early phases of dissociation. To judge from Fig. 4, we prefer to see in it the effect of multiple curve crossings sampled only as the particles separate. To make this clearer, we show in Fig. 5 the dependence on R of the adiabatic energies of the 20 lowest vibrational levels of the two-dimensional model for CH_3I .^{4,26} Since our flux method allows an unambiguous coordinate space assignment of the flux, we conclude that the oscillations seen in Fig. 4 are a manifestation of interference in the exit channel and not in the region in which the initial excitation occurs ($R < 4.5$ bohr). This is further confirmed by the observation that the oscillations begin only after the *total* flux has attained its asymptotic value. As discussed in our previous paper,¹¹ the total flux becomes constant only outside of the Franck-Condon region, once the source term $\chi(R)$ in Eq. (1) has become vanishingly small. Ultimately, as R becomes larger than ~ 7.5 bohr, beyond which point the curve interleaving dies out (Fig. 5), the oscillations in the electronic state fluxes die out also.

Figure 6 displays the asymptotic channel fluxes $|\tau|^2$ for each vibrational level of both the $^3Q_{0+}$ and 1Q_1 states. The vibrational distribution of the $^3Q_{0+}(\text{I}^*)$ products is seen to be much colder than that of the $^1Q_1(\text{I})$ products, in

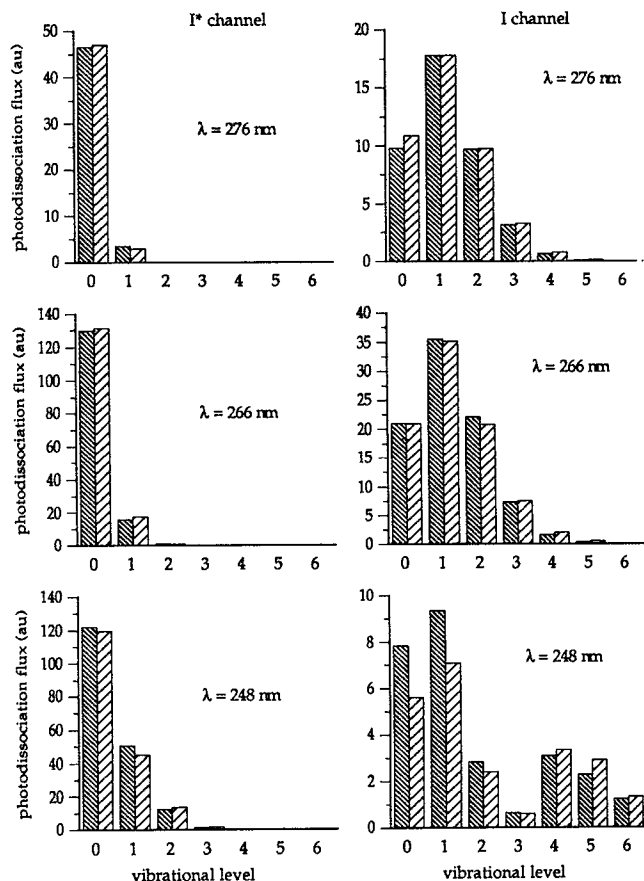


FIG. 6. Histograms representing the asymptotic flux into the vibrational levels of the $^3Q_{0+}(\text{I}^*)$ channel (left panels) and the $^1Q_1(\text{I})$ channel (right panels). Notice that the flux scale changes from one plot to another. The right partner of each histogram represents the results of a fully converged calculation including in the expansion of the wave functions 16 vibrational states for each electronic state and using 230 sectors in the determination of the photodissociation wave function $\chi(R)$. The left partner represents the results of a calculation using only eight vibrational states for each electronic state and only 24 sectors.

expected agreement with the results of the time-dependent study of Guo and Schatz,²⁶ based on the same potential energy surface.

The right-hand partner of each histogram in the six panels in Fig. 6 represents the results of a fully converged calculation, using 230 sectors over the range $3.5 < R < 10$ and using a channel expansion consisting of 16 vibrational states ($0 \leq v < 15$) for each of the two electronic states. The power of the linear reference potential method is illustrated by the left-hand partner of each histogram, which represents the result of a calculation, again ranging from 3.5 to 10 bohr, but with only 24 sectors and only eight vibrational states ($0 \leq v < 7$) included for each of the two electronic states (which was the number of vibrational states included by Shapiro in his original calculation⁴). Despite the drastic reduction in the number of sectors and in the size of the channel basis, the errors in the calculated channel fluxes are no greater than several percent of the total photodissociation flux.

More insight into the mechanism itself is revealed by

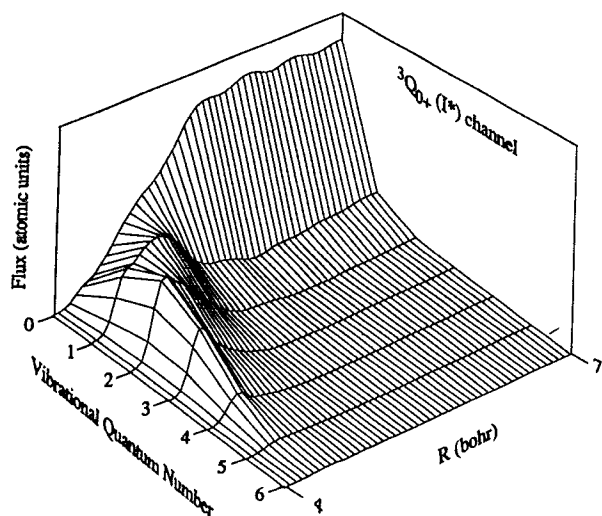


FIG. 7. The flux in the lowest seven vibrational levels of the $^3Q_{0+}(I^*)$ channel as a function of the dissociation coordinate R , for excitation at a wavelength of 266 nm (see Figs. 3 and 4). The sum over all vibrational states gives the total $^3Q_{0+}(I^*)$ flux plotted in the middle panel of Fig. 4. At the largest value of R shown, the fluxes are virtually identical to the asymptotic values plotted in the middle left-hand panel in Fig. 6.

plots of the flux associated with individual product electronic-vibrational states—the $J_n(R_0)$ terms of Eq. (21). These are illustrated in Figs. 7 and 8, for excitation at a wavelength of 266 nm. As can be seen in Fig. 2, Franck–Condon excitation occurs to a region of the $^3Q_{0+}$ surface which lies at somewhat longer r than the equilibrium value in the isolated CH_3 fragment. Furthermore, in the Franck–Condon region, the form of the potential surface is considerably skewed from its behavior at large R . Thus the rising dissociation flux is distributed initially over

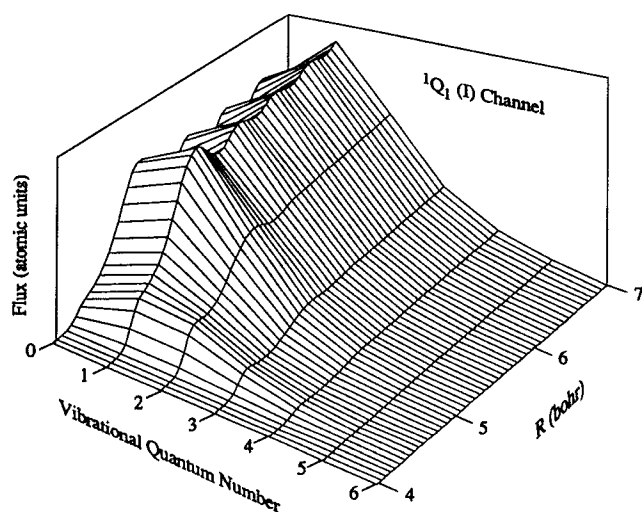


FIG. 8. The flux in the lowest seven vibrational levels of the $^1Q_1(I)$ channel as a function of the dissociation coordinate R , for excitation at a wavelength of 266 nm (see Figs. 3 and 4). The sum over all vibrational states gives the total $^1Q_1(I)$ flux plotted in the middle panel of Fig. 4. At the largest value of R shown, the fluxes are virtually identical to the asymptotic values, plotted in the middle right-hand panel in Fig. 6.

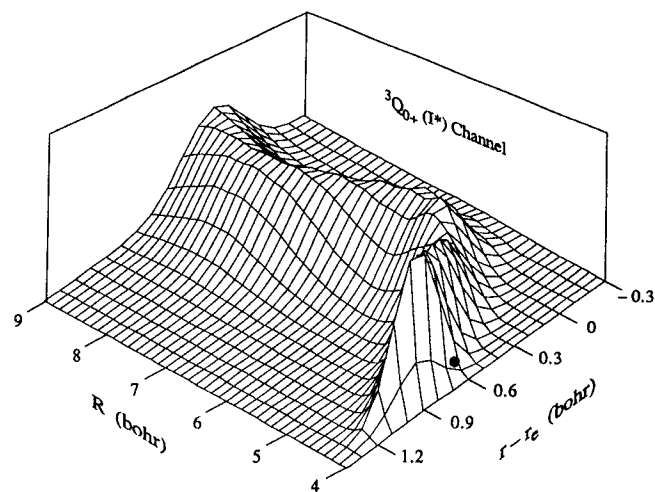


FIG. 9. The photodissociation flux for the $^3Q_{0+}(I^*)$ channel as a function of the dissociation coordinate R and the internal coordinate r of the pseudo-umbrella CH_3 motion for excitation at a wavelength of 266 nm (see Figs. 3 and 4). The Franck–Condon region is centered at $R=4.168$ and $r-r_e=0.618$ bohr, as indicated by the solid circle. The integral over r gives the total $^3Q_{0+}(I^*)$ flux plotted in the middle panel of Fig. 4.

a number of the asymptotic (diabatic) vibrational levels. Quite surprisingly, this vibrationally hot distribution cools dramatically and quickly, so that asymptotically $>87\%$ of the $^3Q_{0+}$ flux appears in the $v=0$ vibrational level. The asymptotic vibrational distribution of the flux is, of course, identical to that shown in the histogram plot in Fig. 6. We observe that the loss of flux out of the $^3Q_{0+}$ state which occurs for R in the range 4.5–5 bohr (see Fig. 4) appears as a loss of flux out of the higher vibrational levels ($v>0$) of this excited electronic state, but is accompanied by an increase in the flux in the $v=0$ level.

We observe (Fig. 8) a slight growth in flux in the 1Q_1 state at $R \approx 4.5$ bohr due to direct photoexcitation at the edge of the Franck–Condon region. However, the region of largest growth in flux in the 1Q_1 state appears at larger R , reflecting the primary mechanism of population of this state by population transfer as the molecules recede through the curve crossing region. Although there is no r -dependent distortion of the 1Q_1 potential energy surface as the $\text{CH}_3\text{--I}$ distance decreases (Fig. 2), the final vibrational distribution in this lower electronic state is nevertheless hotter than in the upper ($^3Q_{0+}$) state. Figures 7 and 8 are the time-independent analogs of the momentum space representations of the dissociating wave packet, which have been advocated recently by Williams and co-workers.⁵⁸

Figures 9 and 10 illustrate plots of the outgoing flux as a function of the vibrational coordinate. The plotted quantities, which are labeled by electronic state, are obtained by integrating the flux given by Eq. (18) over the electronic coordinate alone, which effectively restricts the summation over m and n in Eq. (18) to those channels associated with one or the other electronic state. These plots are the cw time-independent analogs of the time snapshots of wave

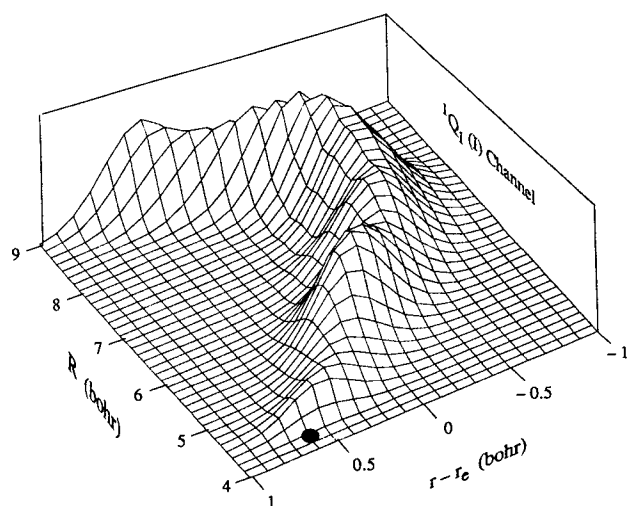


FIG. 10. The photodissociation flux in the ${}^1Q_1(I)$ channel as a function of the dissociation coordinate R and the internal coordinate r of the pseudo-umbrella CH_3 motion for excitation at a wavelength of 266 nm (see Figs. 3 and 4). The Franck-Condon region is centered at $R=4.168$ and $r-r_e=0.618$ bohr, as indicated by the solid circle. The integral over r gives the total ${}^1Q_1(I)$ flux plotted in the middle panel of Fig. 4.

packet motion presented by Guo and Schatz.²⁶ Our time-independent snapshots represent the number of dissociating molecules per unit time which would be seen by a detector placed at coordinates (r, R) . On the other hand, the fixed-time snapshots which result from a time-dependent wave packet calculation measure the time evolution of an initially prepared, spatially localized distribution. However, since the initially prepared wave packet used by Guo and Schatz contains *all* the final energies accessed by the photoexcitation (Fig. 2), the corresponding energy spread is quite large. Thus the information supplied by time snapshots of wave packet motion represents considerable averaging of the monoenergetic information displayed in Figs. 9 and 10.

We observe that the flux distribution plots in Figs. 9 and 10 correspond qualitatively, as one might have anticipated, to a continuous stream of classical particles located initially at the minimum in the ground state surface, which is projected onto the repulsive wall of the excited state surface (Fig. 2) by photon absorption. The particles then slide obliquely down this wall and out the vibrational canyon with some degree of acquired vibrational motion. As discussed by Guo and Schatz,²⁶ and seen clearly in Fig. 6, the degree of vibrational excitation is greater for the fragments emerging in the ${}^1Q_1(\text{CH}_3 + \text{I})$ channel. This greater degree of vibrational excitation is also obvious in the flux distribution plots. The region of electronic nonadiabaticity ($4.5 < R < 5.5$), in which flux is lost from the ${}^3Q_{0+}$ state into the 1Q_1 state, is clearly apparent; once past this region, the overall magnitude of the electronic state fluxes is conserved, while the center of the flux distribution oscillates as a manifestation of the vibrational motion of the CH_3 moiety. We also observe that the initial growth of flux in the ${}^3Q_{0+}$ state occurs at the large- R side of the Franck-Condon region. As in the one-dimensional model (see Fig.

1), at a collision energy of $19\,300\text{ cm}^{-1}$, the ${}^3Q_{0+}$ state is classically forbidden at the minimum in the ground-state potential ($R=4.17$ bohr), so that excitation is induced only by the large- R tail of the ground-state vibrational wave function.

VI. CONCLUSION

In this paper, we have described a new, highly efficient propagator for the time-independent study of molecular photodissociation and the subsequent mechanistic interpretation of this process by the analysis of the photofragment flux redistribution as a function of the fragment separation. The application to a two-dimensional model for the photodissociation of CH_3I is a further demonstration of the power of the analysis of photofragmentation flux redistribution within the framework of the time-independent, driven equation formulation of Band, Freed, and Kouri.¹² The ability to display the flux growth and redistribution in either coordinate space (Figs. 9 and 10) or internal-state space (Figs. 7 and 8) provides a valuable new tool to assist our eventual understanding of the underlying physical mechanism. The graphical demonstrations (Figs. 7–10) of the degree of physical content afforded by application of the flux method to molecular photodissociation contradicts the commonly held belief that time-independent methods applied to molecular photodissociation are less illustrative than time-dependent methods.^{28,59}

The *qualitative* information furnished is similar to that provided by plots of the total photodissociation wave function, as have been presented often by Schinke and co-workers.^{60,61} The advantage of the flux method is twofold. First, the flux distributions connect directly at large R with the experimentally observable quantities, which are the numbers of photofragments appearing in particular internal states per unit time for a given intensity of laser excitation. Indeed, for a given photon frequency ω , the photodissociation cross section from an initial (bound) vibrational level to a particular final state n of the fragments is given by^{11,12}

$$\sigma_n(\omega) = \frac{\omega}{2\epsilon_0 c} |\tau_n(\hbar\omega + E_g)|^2 = \frac{\omega}{2\epsilon_0 c} \lim_{R_0 \rightarrow \infty} J_n(R_0), \quad (36)$$

where E_g is the energy of the bound state and the second equality reiterates Eq. (22). The square of the photodissociation wave function itself $[\psi(R)]^2$ does not have the same direct physical correspondence. Second, the coordinate space flux distributions (Figs. 9 and 10) provide a simpler, more easily grasped picture of the mechanism than comparable plots of the *real* part of the photofragmentation wave function (see, e.g., Refs. 60 and 61) because the latter are overlaid with many nodes due to the highly oscillatory character (in R) of the wave function.

The time-independent analysis of the redistribution of photofragment flux, presented here and in our earlier paper,¹¹ complements the well-established time-dependent wave packet approach to photodissociation.^{15,17–27,49} The direct comparison between the present calculations (Sec. V) and the wave packet calculations of Guo and

Schatz^{26,27} shows well the close similarities. The time-independent flux method will be better suited to the interpretation of single-frequency photodissociation experiments, since the mechanistic information provided by the flux distributions applies to a single energy, while that provided by the study of the time evolution of the initial wave packet represents an average over all the energies accessible in the photoexcitation.

The present article also lays the framework for the analysis of the photofragment flux in an *adiabatic* basis, which represents the internal states of the full Hamiltonian at each interfragment distance R . For problems involving both electronic and nuclear internal degrees of freedom as, e.g., the two-dimensional model of the dissociation of CH_3I investigated in Sec. V, it would ultimately be useful to study the redistribution of photofragment flux in a basis which is *adiabatic* in the vibrational (and/or rotational) degree(s) of freedom, but *diabatic* in the electronic degree of freedom. This will be pursued in future work.

ACKNOWLEDGMENTS

This research was supported by grants to M.H.A. from the National Science Foundation (Grant No. CHE-8917543) and from the U.S. Air Force Office of Scientific Research (Grant No. AFOSR-91-0363) and to D.E.M. from the Science and Engineering Research Council (U.K.). M.H.A. and C.R. would like to thank Susan Marchywka for her help with some technical details of the calculations.

- ¹ M. Shapiro, *J. Chem. Phys.* **56**, 2582 (1975).
- ² Y. B. Band and K. F. Freed, *J. Chem. Phys.* **63**, 3382 (1975).
- ³ K. C. Kulander and J. C. Light, *J. Chem. Phys.* **73**, 4337 (1980).
- ⁴ M. Shapiro, *J. Phys. Chem.* **90**, 3644 (1986).
- ⁵ M. Shapiro and R. Bersohn, *Annu. Rev. Phys. Chem.* **33**, 409 (1982).
- ⁶ G. G. Balint-Kurti and M. Shapiro, *Adv. Chem. Phys.* **60**, 403 (1985).
- ⁷ J. Z. H. Zhang and W. H. Miller, *J. Chem. Phys.* **92**, 1811 (1990).
- ⁸ R. Schinke, *Photodissociation Dynamics* (Cambridge University, Cambridge, England, 1992).
- ⁹ A. Arthurs and A. Dalgarno, *Proc. R. Soc. London, Ser. A* **256**, 540 (1960).
- ¹⁰ See, e.g., D. Secrest, in *Atom-Molecule Collision Theory: A Guide for the Experimentalist*, edited by R. B. Bernstein (Plenum, New York, 1979), p. 265.
- ¹¹ D. E. Manolopoulos and M. H. Alexander, *J. Chem. Phys.* (in press).
- ¹² Y. B. Band, K. F. Freed, and D. J. Kouri, *J. Chem. Phys.* **74**, 4380 (1981).
- ¹³ M. H. Alexander, *J. Chem. Phys.* **95**, 8931 (1991).
- ¹⁴ M. H. Alexander, *J. Chem. Phys.* **96**, 6672 (1992).
- ¹⁵ K. C. Kulander and E. J. Heller, *J. Chem. Phys.* **69**, 2439 (1978).
- ¹⁶ S. Y. Lee and E. J. Heller, *J. Chem. Phys.* **71**, 4777 (1979).
- ¹⁷ E. J. Heller, *Acc. Chem. Res.* **14**, 368 (1981).
- ¹⁸ R. N. Dixon, *Mol. Phys.* **54**, 333 (1985).
- ¹⁹ R. H. Bisseling, R. Kosloff, and J. Manz, *J. Chem. Phys.* **83**, 93 (1985).
- ²⁰ R. D. Coalson and J. L. Kinsey, *J. Chem. Phys.* **85**, 4322 (1986).
- ²¹ S. Das and D. J. Tannor, *J. Chem. Phys.* **91**, 2342 (1989).
- ²² S. K. Gray and C. E. Wozny, *J. Chem. Phys.* **91**, 7671 (1989).
- ²³ X.-P. Xiang, R. Heather, and H. Metiu, *J. Chem. Phys.* **90**, 6903 (1989).
- ²⁴ K. Kulander, C. Cerjan, and A. E. Orel, *J. Chem. Phys.* **94**, 571 (1991).
- ²⁵ R. Schinke, K. Weide, B. Heumann, and V. Engel, *Faraday Discuss. Chem. Soc.* **91**, 31 (1991).
- ²⁶ H. Guo and G. C. Schatz, *J. Chem. Phys.* **93**, 393 (1990).
- ²⁷ H. Guo and G. C. Schatz, *J. Phys. Chem.* **95**, 3091 (1991).
- ²⁸ C. J. Williams, J. Qian, and D. J. Tannor, *J. Chem. Phys.* **95**, 1721 (1991).
- ²⁹ J. H. Frederick, E. J. Heller, J. L. Ozment, and D. W. Pratt, *J. Chem. Phys.* **88**, 2169 (1988).
- ³⁰ B. R. Johnson, *J. Comp. Phys.* **13**, 445 (1973).
- ³¹ F. Mrugała and D. Secrest, *J. Chem. Phys.* **78**, 5954 (1983).
- ³² F. Mrugała and D. Secrest, *J. Chem. Phys.* **79**, 5960 (1983).
- ³³ D. E. Manolopoulos, *J. Chem. Phys.* **85**, 6425 (1986).
- ³⁴ D. E. Manolopoulos, Ph. D. thesis, University of Cambridge, 1988.
- ³⁵ M. H. Alexander, G. Parlant, and T. Hemmer, *J. Chem. Phys.* **91**, 2388 (1989).
- ³⁶ D. E. Manolopoulos, M. J. Jamieson, and A. D. Pradhan, *J. Comput. Phys.* (in press).
- ³⁷ F. Mrugała, *J. Comput. Phys.* **58**, 113 (1985).
- ³⁸ F. Mrugała, *J. Chem. Phys.* **91**, 874 (1989).
- ³⁹ F. Calogero, *Variable Phase Approach to Potential Scattering* (Academic, New York, 1967), Appendix I.
- ⁴⁰ R. G. Gordon, *J. Chem. Phys.* **51**, 14 (1969).
- ⁴¹ R. G. Gordon, *Methods Comput. Phys.* **10**, 81 (1971).
- ⁴² M. H. Alexander and D. E. Manolopoulos, *J. Chem. Phys.* **86**, 2044 (1987).
- ⁴³ R. G. Gordon, *J. Chem. Phys.* **52**, 6211 (1970).
- ⁴⁴ M. H. Alexander (to be published).
- ⁴⁵ W. H. Miller, S. D. Schwartz, and J. W. Tromp, *J. Chem. Phys.* **79**, 4889 (1983).
- ⁴⁶ J. W. Tromp and W. H. Miller, *Faraday Discuss. Chem. Soc.* **84**, 441 (1987).
- ⁴⁷ If the outgoing waves in Eq. (5) are normalized by the square root of the channel wave vector (Ref. 10), then the units of τ will be length^{-1} , and the relationship between τ and the asymptotic flux [Eq. (22)] becomes $J_n(\infty) = \hbar |\tau_n|^2 / \mu$.
- ⁴⁸ R. Schinke, *J. Chem. Phys.* **85**, 5049 (1986).
- ⁴⁹ H. Guo, K. Q. Lao, G. C. Schatz, and A. D. Hammerich, *J. Chem. Phys.* **94**, 6562 (1991).
- ⁵⁰ S.-Y. Lee and E. J. Heller, *J. Chem. Phys.* **76**, 3035 (1982).
- ⁵¹ T. F. Hunter and K. S. Krisjansson, *Chem. Phys. Lett.* **58**, 291 (1978).
- ⁵² S. L. Baughcum and S. R. Leone, *J. Chem. Phys.* **76**, 6531 (1980).
- ⁵³ P. Brewer, P. Das, G. Ondrey, and R. Bersohn, *J. Chem. Phys.* **79**, 720 (1983).
- ⁵⁴ G. N. A. van Veen, T. Baller, A. E. deVries, and N. J. A. van Veen, *Chem. Phys.* **87**, 405 (1984).
- ⁵⁵ M. D. Barry and P. A. Gorry, *Mol. Phys.* **52**, 461 (1984).
- ⁵⁶ W. P. Hess, S. J. Kohler, H. K. Haugen, and S. R. Leone, *J. Chem. Phys.* **84**, 2143 (1986).
- ⁵⁷ M. S. Child, *Molecular Collision Theory*, 2nd ed. (Academic, New York, 1974).
- ⁵⁸ C. J. Williams, J. Qian, and D. J. Tannor, *J. Chem. Phys.* **95**, 1721 (1992).
- ⁵⁹ A. Untch, K. Weide, and R. Schinke, *J. Chem. Phys.* **95**, 6496 (1991).
- ⁶⁰ R. Schinke, *J. Chem. Phys.* **92**, 2397 (1990).
- ⁶¹ R. Schinke, A. Untch, H. U. Suter, and J. R. Huber, *J. Chem. Phys.* **94**, 7929 (1991).